

ISTITUTO NAZIONALE DI RICERCA METROLOGICA Repository Istituzionale

Magnetic losses versus sintering treatment in Mn-Zn ferrites

This is the author's submitted version of the contribution published as:

Original

Magnetic losses versus sintering treatment in Mn-Zn ferrites / Beatrice, Cinzia; Tsakaloudi, Vasiliki; Dobák, Samuel; Zaspalis, Vassilios; Fiorillo, Fausto. - In: JOURNAL OF MAGNETISM AND MAGNETIC MATERIALS. - ISSN 0304-8853. - 429:(2017), pp. 129-137. [10.1016/j.jmmm.2016.12.121]

Availability:

This version is available at: 11696/54953 since: 2021-01-28T14:47:27Z

Publisher:

Elsevier

Published

DOI:10.1016/j.jmmm.2016.12.121

Terms of use:

This article is made available under terms and conditions as specified in the corresponding bibliographic description in the repository

Publisher copyright

(Article begins on next page)

Magnetic losses versus sintering treatment in Mn-Zn Ferrites

Cinzia Beatrice^{1*}, Vasiliki Tsakaloudi², Samuel Dobák³, Vassilios Zaspalis⁴, Fausto Fiorillo¹

¹Istituto Nazionale di Ricerca Metrologica, Nanoscience and Materials Division, Torino, Italy

²Laboratory of Inorganic Materials, CERTH, Themi-Thessaloniki, Greece

³Institute of Physics, P.J. Šafárik University, Košice, Slovakia

⁴Department of Chemical Engineering Aristotle University of Thessaloniki, Thessaloniki, Greece

ABSTRACT

Mn-Zn ferrites prepared by different sintering schedules at 1325 °C, 1340 °C, and 1360 °C, have been characterized from the structural, electrical, and magnetic viewpoint. Magnetic losses and complex permeability have been, in particular, measured and analyzed from quasi-static excitation up to 1 GHz. It is observed that lower sintering temperatures and shorter times lead to more homogeneous grain structure and better soft magnetic response at all frequencies. It is shown, however, that, once the contribution by eddy currents is singled out, the energy losses tend to coincide beyond a few MHz in the differently treated samples. The interpretative approach consists in separating the contributions by the domain wall displacements and the magnetization rotations to complex permeability and losses as a function of frequency. This can be accomplished in a relatively simple way upon the low induction region consistent with the Rayleigh law, where these quantities can be quantitatively related and the linear Landau-Lifshitz-Gilbert equation applies, account being taken of the distribution in amplitude and orientation of the local anisotropy fields.

Keywords—Mn-Zn ferrites, Magnetic losses, Complex permeability, Landau-Lifshitz equation.

* Corresponding author: c.beatrice@inrim.it

I. INTRODUCTION

Excellent broadband permeability response and low losses are basic requirements for modern Mn-Zn ferrites. These properties are pursued using high-quality raw materials and acting on composition and microstructure. Thus, by suitable excess of Fe^{2+} ions one can minimize the magnetocrystalline anisotropy [1], while the resistivity of the material can be increased by calibrated additions of impurities (e.g. CaO , SiO_2 , Nb_2O_5 , etc.) [2]. Optimal control of microstructure is more complex, because of its governing role on the magnetization process and its manifold behavior. It is, for example, generally accepted that permeability dispersion can move to higher frequencies by reducing the grain size, at the cost of reduced DC permeability [3][4][5], but contrasting assumptions regarding the structure related mechanisms responsible for the magnetic losses, their evolution with frequency and the related behavior of the complex permeability are adopted in the literature. On the one hand, the respective roles of domain wall (d.w.) processes and magnetization rotations have been variously interpreted, assuming either resonant or relaxation response versus frequency, while pointing out, at the same time, the difficulty of experimentally separating the related contributions. For example, permeability dispersion in polycrystalline and composite Mn-Zn ferrites up to about 1 GHz has been interpreted by a number of authors through combination of resonant d.w. response and relaxation by rotations [6][7][8]. Domain wall resonance is then often assumed to chiefly contribute to the high-frequency losses, the so-called “residual losses” [9][10]. Experimental evidence exists, however, for concluding that the d.w. motion in Mn-Zn ferrites has relaxation character, with cutoff frequency around 1 MHz or lower [11]. Further difficulties in relating structure and losses arise in connection with the electrical properties of the heterogeneous polycrystalline Mn-Zn ferrites (semiconducting grains and insulating boundary layers), the ensuing evolution of the eddy current paths with frequency, and the calculation of the eddy current losses [12].

In recent years, comprehensive experiments on commercial ferrites have provided solid background for a consistent interpretative assessment of permeability dispersion and magnetic losses from DC to radiofrequencies [13][14][15]. It is based, besides the conventional separation between quasi-static (hysteresis) and dynamic losses, on the identification and calculation of the classical eddy current losses, experimentally validated by measurements as a function of sample thickness [14]. The d.w. and the rotational contributions are then separated, the latter being obtained by calculating the real and imaginary susceptibility components versus frequency as solutions of the Landau-Lifshitz-Gilbert equation, suitably integrated versus the distribution of the local anisotropy fields.

In this work we have investigated the effect of different sintering schedules at 1325 °C, 1340 °C, and 1360 °C on the broadband (DC – 1 GHz) magnetic loss $W(f)$ and permeability $\mu = \mu' - j\mu''$ behavior of $\text{Mn}_{0.821}\text{Zn}_{0.179}\text{Fe}_2\text{O}_4$ ring samples and interpreted it according to the previously mentioned theoretical framework. It is observed that higher sintering temperatures, leading to larger grains and generally lower resistivity, are detrimental to loss and permeability at all frequencies. It is remarkably found, however,

that, eddy current losses play a role in the measured ring samples (5.0 mm × 2.5 mm cross-sectional area) only beyond a few MHz. Once they are suppressed by thickness reduction, all the $W(f)$ curves tend to collapse on a single curve at high frequencies. It will then be shown in the following how the loss and permeability phenomenology can be assessed in terms of dominant d.w. dynamics and rotational processes and the related spin damping dissipation in the lower and upper range of frequencies, respectively.

II. EXPERIMENTAL PROCEDURE

The starting Mn-Zn ferrite powder was prepared by the conventional ceramic method of solid state reaction. The high purity raw materials (Merck), consisting of 70 wt % Fe_2O_3 , 24 wt % MnO and 6 wt % ZnO , were weighed in the right proportions to give a batch of 500 g and were dry-mixed using a lab mixer. The oxides mixture was pre-fired at 800°C in air and the crystal structure of the pre-fired powder was determined by X-ray Diffraction. Typical dopants, such as Nb_2O_5 and CaO [16] were introduced into the pre-fired powder and ball milling was applied for 8 hours, using steel vessels. The particle size distribution of the milled powder was determined by laser scattering (Malvern Mastersizer S). Roll granulation of the milled powder was performed using a rotating drum with the addition of 0.2 wt % of aqueous solution of polyvinyl alcohol (Merck, Analytical Grade, MW72000). The Mn-Zn ferrite granulated powders were pressed using an isostatic hydraulic press and the toroidal specimens of external diameter of 16.8 mm, internal diameter of 8.4 mm and height of 6 mm were measured to have a press density of $2.90 \pm 0.02 \text{ g/cm}^3$. Sintering was performed in specially constructed programmable kilns following the oxygen partial pressure equilibrium proposed by Morineau and Paulus [17]. Different sintering schedules were performed at the temperatures $T_s = 1325^\circ\text{C}$, 1340°C , and 1360°C for times $t_s = 3$ hours, 5 hours, and 7 hours at top temperature. The Archimedes' method was followed to measure the sinter density of the final ring specimens. These had outside diameter (D_o), inside diameter (D_i) and thickness (d) in the ranges: 14.54 mm – 14.64 mm (D_o), 9.28 mm – 9.36 mm (D_i), 4.86 mm – 5.16 mm (d). The magnetic path length was calculated as $l_m = \pi(D_o - D_i) / \ln(D_o / D_i)$. The polycrystalline microstructure of the sintered specimens was evaluated by Scanning Electron Microscopy (SEM-Jeol 6300) on the ground, polished and chemically etched toroidal specimens coming from each of the sintering trials.

The real ρ' and imaginary ρ'' resistivity components of the investigated Mn-Zn ferrites were obtained up to about 15 MHz by means of standard four-wire measurements of the electrical impedance of cut rings, where voltmetric and amperometric electrical contacts are made by sandwiching indium strips between the freshly polished sample surface and the copper leads and applying uniform pressure. Details of the measuring procedure are given in [14][15]. $\rho'(f)$ and $\rho''(f)$ show well known behaviors, with $\rho'(f)$ decreasing with f and $\rho''(f)$ displaying a capacitive character, according to an equivalent RC circuit [19]. At low frequencies $\rho'(f)$ is chiefly determined by the near-insulating grain boundaries, while the plateau

appearing in the $\rho'(f)$ curve at high frequencies (beyond about 1 MHz) directly provides the resistivity of the grains [14][15].

The magnetic characterization was performed up to 10 MHz by fluxmetric measurements, based on the use of a calibrated hysteresisgraph-wattmeter. The primary and secondary windings, their layout, and the connecting cables ensured minimum spurious effects due to the stray capacitances. The high-frequency measurements, from a few hundred kHz to 1 GHz, were covered by a transmission line method, where the impedance of the ferrite sample placed at the bottom of a shorted coaxial cable was obtained by measuring the reflection scattering parameter by an Agilent 8753A Vector Network Analyzer (VNA, 10 mW irradiated power). Details on the magnetic characterization methods are provided in [14][18].

III. BASIC PROPERTIES VERSUS SINTERING TREATMENT.

The SEM investigation shows broadening distribution and larger mean value $\langle s \rangle$ of the grain size on increasing the sintering temperature T_s , as illustrated by the example shown in Fig. 1. Homogeneous grain growth is observed for $T_s = 1325$ °C and $T_s = 1340$ °C with some residual porosity. Increasing T_s to 1360 °C somewhat exceeds the optimal conditions for homogeneous grain growth and incipient secondary re-crystallization is observed. This is especially important upon the 7-hour treatment, as demonstrated by the corresponding irregular grain size distribution shown in Fig. 1. Significant internal stresses are therefore introduced. Extensive characterization shows then that the soft magnetic properties moderately deteriorate, for a given T_s value, by increasing the sintering time t_s and, for a same t_s value, on increasing T_s . This is illustrated by the example shown in Fig. 2, providing a general overview of the dependence of the energy loss on T_s and t_s in all the developed materials at 100 kHz and peak polarization $J_p = 100$ mT. Significant differences are found between the two extreme conditions: $t_s = 3$ hours at $T_s = 1325$ °C (sample A) and $t_s = 7$ hours at $T_s = 1360$ °C (sample I). These two cases will be analyzed in full detail in the following, together with results obtained on samples subjected to the intermediate treatments $t_s = 3$ hours at $T_s = 1340$ °C (sample D) and $t_s = 3$ hours at $T_s = 1360$ °C (sample G). Table 1 summarizes the main physical properties of the so selected ferrites. Fig. 3 compares the normal magnetization curves of the samples A, I, and G. The detrimental effect of higher sintering temperatures and longer times is apparent. To note that the Rayleigh law $\mu(H) = a + bH$, with a (the initial permeability) and b constants applies up to the polarization $J_p \sim 60$ mT (hatched region in Fig. 3). Because of the low value of the anisotropy constant, rotational processes are expected to contribute to good extent to the initial permeability. We will see in the following how, based on simple assumptions, one can calculate such a contribution. We can state in any case that the irreversible term bH is only due to the d.w. motion. A comparison of the energy loss behaviors at $J_p = 10$ mT in the same samples from a few hundred Hz (quasi-static excitation) up to 1 GHz is shown in Fig. 4a. This broad frequency range is achieved by combination of the direct fluxmetric measurements at defined J_p and the transmission line (TL) measurements at given output power of the VNA. The latter provides, via the

reflection scattering parameter S_{11} , the real μ' and imaginary μ'' permeability components under given power of the electromagnetic wave. It is remarkably found, at least within the Rayleigh region, that beyond a certain frequency these quantities become independent of J_p and, as shown in Fig. 4b, fluxmetric and TL curves collapse on a single curve. Consequently, the energy loss at a given J_p value is derived as

$$W(J_p, f) = \pi J_p^2 \mu''(f) / (\mu'^2(f) + \mu''^2(f)). \quad [\text{J/m}^3] \quad (1)$$

The high-frequency loss curves in Fig. 4a, obtained in this way, superpose with the fluxmetrically measured losses (symbols) beyond about 3 MHz. The overlapping frequency span increases with decreasing J_p . We thus observe, for example, in Fig. 5 (samples I and D), that fluxmetric and TL curves match already around 500 kHz at $J_p = 2$ mT. This is physically justified in terms of a correspondingly increasing role of the rotations with respect to the d.w. displacements upon decreasing J_p . Rotations respond to good approximation linearly within the Rayleigh region and the corresponding permeability contribution is independent of J_p . We thus find the behaviors of μ' and μ'' shown in the example of Fig. 6, concerning the sample A. It is observed here how the fluxmetric results (symbols) superpose with the TL curve to the largest extent at $J_p = 2$ mT.

An overall comparison of the broadband energy loss $W(f)$ behaviors measured in the samples A and I for J_p ranging between 2 mT and 200 mT is given in Fig. 7. The more irregular and defective structure of the I sample, with its additional magnetostrictive effects, is conducive to the observed higher energy losses at low and intermediate frequencies, consistent with the behavior of the magnetization curves (Fig. 3). With the d.w. processes relaxing in the MHz range, the loss curves in the two samples tend to coalesce, with a barely noticeable difference remaining at the highest frequencies. This is related to a correspondingly different high-frequency conductivity (see Table 1).

IV. DISCUSSION

A rational approach to the broadband energy loss and permeability properties of the Mn-Zn ferrites calls for assessment of the involved magnetization processes, the d.w. displacements and the magnetization rotations, and distinction between the intrinsic dissipation mechanisms, i.e. eddy currents and spin damping. Qualitative approaches to the separate d.w. and rotational contributions to the permeability and its frequency behavior have been proposed in the literature, with contrasting conclusions regarding the nature of the dispersion (relaxation versus resonance) and the correspondingly covered frequency ranges [6][8][11]. To implement such a separation, which provides a highly schematic view of the complexity of the actual physical process, certain simplifying assumptions are in order. Basically, we consider both the real and the imaginary permeability components as the sum of d.w. and rotational components, according to the expression

$$\mu = \mu' - j\mu'' = (\mu'_{\text{dw}} + \mu'_{\text{rot}}) - j(\mu''_{\text{dw}} + \mu''_{\text{rot}}). \quad (2)$$

We thus assume that the energy loss $W(f)$ can be expressed as the sum of d.w. and rotational contributions, so that for a given value H_p of the applied peak field we have, under the linear approximation, $W(f) = \pi H_p^2 (\mu'_{dw}(f) + \mu''_{rot}(f))$. In previous papers, we proposed a method for singling out the d.w. permeability components μ'_{dw} and μ''_{dw} versus frequency and peak polarization. It relied on measurements of disaccommodation, a phenomenon exclusively affecting the d.w. motion [14][15]. In this work we discuss a simpler approach, based on the idea that, within the previous low-induction limit (Fig. 3), the rotational permeability is independent of J_p , because the increase of permeability versus J_p (the linear term in the Rayleigh law) is exclusively generated by the d.w. processes. The difference between two permeability versus frequency curves at two generic polarization values J_{p1} and J_{p2} , with $J_{p1} > J_{p2}$, can therefore be expressed as

$$\mu'(J_{p1}, f) - \mu'(J_{p2}, f) = \mu'_{dw}(J_{p1}, f) - \mu'_{dw}(J_{p2}, f), \quad (3)$$

the difference between the corresponding d.w. contributions. The same is assumed to hold for $\mu''(J_p, f)$. In addition, the low-frequency portion of μ'' (the flat part of the curves in Fig. 6b) coincides with μ''_{dw} , because, being directly related to the hysteresis (quasi-static) energy loss, is d.w. generated. We see here how μ''_{dw} and μ''_{rot} can be obtained by the measured permeability by simple iteration. Let us therefore consider, for example, the J_p interval 2 mT-50mT in sample A and, in particular, the difference

$$\mu''(50 \text{ mT}, f) - \mu''(2 \text{ mT}, f) = \mu''_{dw}(50 \text{ mT}, f) - \mu''_{dw}(2 \text{ mT}, f). \quad (4)$$

Since $\mu''_{dw}(2 \text{ mT}, f) \ll \mu''_{dw}(50 \text{ mT}, f)$, we pose at first $\mu''(50 \text{ mT}, f) - \mu''(2 \text{ mT}, f) \cong \mu''_{dw}(50 \text{ mT}, f)$ and obtain the rotational permeability as $\mu''_{rot}(f) \cong \mu''(50 \text{ mT}, f) - \mu''_{dw}(50 \text{ mT}, f)$. The approximate value $\mu''_{dw}(2 \text{ mT}, f) \cong \mu''(2 \text{ mT}, f) - \mu''_{rot}(f)$ is then obtained and inserted again in (4), thereby providing a new value for $\mu''_{dw}(50 \text{ mT}, f)$ and $\mu''_{rot}(f)$. A couple of iterations usually suffice for convergence. For a generic J_p value we thus obtain $\mu''_{dw}(J_p, f) = \mu''(J_p, f) - \mu''_{rot}(f)$. The $\mu''(J_p, f)$ behaviors in sample A shown in Fig. 6 are then interpreted in terms of combination of the components $\mu''_{dw}(J_p, f)$ and $\mu''_{rot}(f)$, as illustrated in Fig. 8a for $J_p = 2 \text{ mT} - 50 \text{ mT}$. The real component $\mu'_{dw}(2 \text{ mT}, f)$ is also shown in this figure. It is estimated from knowledge of the imaginary component $\mu''_{dw}(2 \text{ mT}, f)$ according to the relaxation formula $\mu'_{dw}(2 \text{ mT}, f) = 2 \cdot \mu''(2 \text{ mT}, f_{\max}) / (1 + (f / f_{\max})^2)$, where f_{\max} is the frequency at which $\mu''_{dw}(2 \text{ mT}, f)$ is maximum (about 1.1 MHz in this sample). This somewhat ideal derivation, consistent with the finding by Eq. (3) that μ'_{dw} has relaxation character, contains an obvious degree of approximation,

but permits one to outrightly calculate $\mu'_{\text{dw}}(J_p, f)$ (at least up to $J_p = 50$ mT) through Eq. (3) and $\mu'_{\text{rot}}(f) = \mu'(J_p, f) - \mu'_{\text{dw}}(J_p, f)$. Fig. 8b shows how the initial permeability is dominated by the rotations, the sole process surviving at the highest frequencies, whose resonant character is apparent from the shape of $\mu'_{\text{rot}}(f)$. The same decomposition procedure applied to the measurements on sample I leads to the results shown in Figs. 9 and 10. Higher d.w and rotational permeabilities are found in sample A, consistent with the behavior of the initial magnetization curves in the Rayleigh region (Fig. 3). Looking then at the rotational permeability, its higher low-frequency value in sample A ($\mu'_{\text{rot,DC}} = 1620$ vs. $\mu'_{\text{rot,DC}} = 1200$) is partially compensated by higher center resonance frequency in sample I ($f_0 = 3$ MHz vs. $f_0 = 2.6$ MHz in sample A). Slightly higher Snoek's product is however associated with sample A (4.2 GHz vs. 3.6 GHz).

Eq. (1) shows that, within the previous low-induction limits, permeability and energy loss are in a direct relationship. The previous analysis additionally brings to light the conspicuous role of μ'_{rot} and μ''_{rot} in the upper frequency range, which are found to basically coincide with μ' and μ'' above about 1 MHz. The rotational losses, however, may result from two concurring dissipation mechanisms: eddy currents and spin-damping. Eddy currents are duly considered in developing Mn-Zn ferrites and, as with the present materials, they are effectively countered by oxide dopants segregating at the grain boundaries. However, since the grain boundary resistivity becomes ineffective on approaching the MHz range (the measured resistivity in our samples decreasing from the DC value of 5-7 Ωm to about 0.02 Ωm at 1 MHz) eddy current losses could play a role at high frequencies, depending on sample size. We have indeed remarked in Fig. 4 that slight differences, connected with the measured high-frequency conductivities (Table 1), occur beyond a few MHz in the energy loss versus frequency curves of the A, G, and I samples.

In previous works we have developed a model for eddy current losses in Mn-Zn ferrites, which could be described according to a classical approach, taking into account the inhomogeneous structure of the material [14][15]. It was shown that with this model, applied to Mn-Zn ring samples of different size, one could eventually retrieve by subtraction the eddy-current-free energy loss curves, coinciding with the curves measured on sufficiently thin samples [14]. These limiting curves have been obtained in the present samples by progressively reducing by grinding their thickness down to about 1.2 mm, as illustrated by the example shown in Fig. 11. Here the $W(f)$ curves taken at $J_p = 2$ mT in the starting 5 mm thick samples A and I, which slightly differed at the highest frequencies, are modified upon thinning beyond about 5 MHz because of the disappearance of the eddy current loss $W_{\text{eddy}}(f)$. They collapse then into a single curve beyond such a frequency. This a curve we shall analyze across the whole frequency range in terms of combination of d.w. and rotational contributions. To start with, we describe the viscous rotational response of the spins inside the magnetic domains to the applied AC field by the Landau-Lifshitz-Gilbert (LLG) equation. For the specific case of a domain where the anisotropy field H_k is normal to the exciting alternating field, the LLG equation provides the susceptibilities

$$\chi'_{\text{rot}}(\omega, H_k) = \frac{\gamma^2 \mu_0^2 H_k M_s [\gamma^2 \mu_0^2 H_k^2 - (1 - \alpha_{\text{LL}}^2) \omega^2]}{[\gamma^2 \mu_0^2 H_k^2 - (1 + \alpha_{\text{LL}}^2) \omega^2]^2 + 4 \alpha_{\text{LL}}^2 \gamma^2 \mu_0^2 H_k^2 \omega^2} \quad (5a)$$

$$\chi''_{\text{rot}}(\omega, H_k) = \frac{\omega \alpha_{\text{LL}} \gamma \mu_0 H_k M_s [\gamma^2 \mu_0^2 H_k^2 + (1 + \alpha_{\text{LL}}^2) \omega^2]}{[\gamma^2 \mu_0^2 H_k^2 - (1 + \alpha_{\text{LL}}^2) \omega^2]^2 + 4 \alpha_{\text{LL}}^2 \gamma^2 \mu_0^2 H_k^2 \omega^2}, \quad (5b)$$

where $\omega = 2\pi f$, γ is the electron gyromagnetic ratio, M_s is the saturation magnetization, and α_{LL} is the Landau-Lifshitz damping factor. In the limit $\omega = 0$, $\chi'_{\text{rot}} = M_s/H_k$. The associated dissipation mechanism is the release of energy from the precessing spins to the lattice by spin wave decay into the system of lattice vibrations [20]. For a polycrystalline soft ferrite we may assume that the intergrain demagnetizing fields can significantly interfere with the magnetocrystalline anisotropy fields, which have relatively low values, giving rise to a distribution $g(H_{k,\text{eff}})$ of effective anisotropy fields $H_{k,\text{eff}}$. An orientation distribution $p(\theta)$ for the easy axes should also be considered, resulting in the average susceptibilities

$$\langle \chi'_{\text{rot}}(f) \rangle = \int_0^\infty g(H_{k,\text{eff}}) dH_{k,\text{eff}} \int_0^{\pi/2} p(\theta) d\theta \chi'_{\text{rot}}(f, H_{k,\text{eff}}, \theta) \quad (6a)$$

$$\langle \chi''_{\text{rot}}(f) \rangle = \int_0^\infty g(H_{k,\text{eff}}) dH_{k,\text{eff}} \int_0^{\pi/2} p(\theta) d\theta \chi''_{\text{rot}}(f, H_{k,\text{eff}}, \theta), \quad (6b)$$

where the assumed isotropic distribution in the half-space of the angle θ made by the easy axis with the direction of the AC field is $p(\theta) = \sin\theta$. Posing then $\chi'_{\text{rot}}(f, H_{k,\text{eff}}, \theta) = \chi'_{\text{rot}}(f, H_{k,\text{eff}}) \cdot \sin^2 \theta$ and $\chi''_{\text{rot}}(f, H_{k,\text{eff}}, \theta) = \chi''_{\text{rot}}(f, H_{k,\text{eff}}) \cdot \sin^2 \theta$ and integrating over the angular distribution, we obtain

$$\langle \chi'_{\text{rot}}(f) \rangle = \frac{2}{3} \int_0^\infty g(H_{k,\text{eff}}) \chi'_{\text{rot}}(f, H_{k,\text{eff}}) dH_{k,\text{eff}} \quad (7a)$$

$$\langle \chi''_{\text{rot}}(f) \rangle = \frac{2}{3} \int_0^\infty g(H_{k,\text{eff}}) \chi''_{\text{rot}}(f, H_{k,\text{eff}}) dH_{k,\text{eff}}. \quad (7b)$$

A lognormal distribution function is taken for $g(H_{k,\text{eff}})$

$$g(H_{k,\text{eff}}) = \frac{1}{\sqrt{2\pi} \sigma H_{k,\text{eff}}} \cdot \exp\left[-\frac{(\ln(H_{k,\text{eff}}) - h)^2}{2\sigma^2}\right], \quad (8)$$

where $h = \langle \ln(H_{k,\text{eff}}) \rangle$ and σ is the standard deviation of $\ln(H_{k,\text{eff}})$. To simplify the matter, we introduce the field $H_{k0} = \exp(h)$. It is remarked that, as the grains associated with lower anisotropy field pass through resonance, they become transparent to the AC field and unable to compensate the magnetic poles appearing on the surrounding grains, whose resonance frequency will on the average be raised. We can associate to a generic grain merged in a medium of quasi-static susceptibility $\chi(f)$ an effective demagnetizing coefficient $N_{d,\text{eff}} \sim N_d / (1 + \chi(f))$. At sufficiently high frequencies $\chi(f)$ will decrease and we can assume that the local demagnetizing field will correspondingly increase on the average by a quantity

$\Delta H_d \propto \Delta N_{d,\text{eff}} \approx \frac{N_d}{\chi_{\text{DC}}} \cdot \frac{\chi_{\text{DC}} - \chi(f)}{1 + \chi(f)}$. Consequently, the distribution $g(H_{k,\text{eff}})$ will widen towards higher $H_{k,\text{eff}}$

values, following the decrease of the total susceptibility $\chi(f)$ with frequency, an effect lumped in the frequency dependence of the quantity h , according to $h(f) = \ln(H_{k0}^{(\text{DC})} + C \cdot \frac{\chi_{\text{DC}} - \chi(f)}{1 + \chi(f)})$, with C a constant.

The rotational susceptibilities given by Eqs. 5a and 5b have been calculated with $\alpha_{\text{LL}} = 0.04$ and integrated according to Eqs. 7a and 7b. The term h in the distribution (8) becomes dependent on f beyond a few MHz. From the so calculated $\mu'_{\text{rot}}(f) = 1 + \chi'_{\text{rot}}(f)$ and $\mu''_{\text{rot}}(f) = \chi''_{\text{rot}}(f)$, the rotational loss $W_{\text{rot}}(f)$ is obtained applying Eq. (1). The d.w. contribution $W_{\text{dw}}(f)$ is then obtained subtracting $W_{\text{rot}}(f)$ to the measured energy loss $W(f)$. Fig. 12 provides an example of the so predicted loss decomposition $W(f) = W_{\text{dw}}(f) + W_{\text{rot}}(f)$ at two J_p values in the 1.25 mm thin (eddy-current-free) sample A. $\chi'_{\text{rot}}(f)$ and $\chi''_{\text{rot}}(f)$ have been calculated using the following parameters in the distribution $g(H_{k,\text{eff}})$: $\sigma = 1.2$, $H_{k0}^{(\text{DC})} = 250$ A/m, $C = 7$. It is noted how the sharp increase of the measured $W(f)$ for $J_p = 2$ mT is associated with a surge of the rotational losses on entering the frequency domain (above a few hundred kHz) where resonant energy absorption starts to occur. This effect is smoothed out at $J_p = 20$ mT, because of the increased proportion of $W_{\text{dw}}(f)$ at low and medium frequencies. It can then be stated that at the highest investigated J_p values of 100 mT and 200 mT, $W(f) \sim W_{\text{dw}}(f)$ up to about 1 MHz, that is, upon the frequency range of interest in power electronics. Here the concept of excess loss should apply to describe the dynamic behavior of $W_{\text{dw}}(f)$ [13] [21]. $W_{\text{rot}}(f)$ in sample I was obtained with $H_{k0}^{(\text{DC})} = 290$ A/m and $C = 20$, the other parameters unchanged. The latter prediction is directly connected with the calculation via Eqs. (7a) and (7b) of $\mu'_{\text{rot}}(f)$ and $\mu''_{\text{rot}}(f)$ shown in Fig. 13.

V. CONCLUSION

Mn-Zn ferrites sintered for 3, 5, and 7 hours at 1325 °C, 1340 °C, and 1360 °C show broadening distribution of the grain size with increasing treatment temperatures and time, with associated moderate worsening of the quasi-static soft magnetic properties. Detrimental effects appear, in particular, to derive from partial secondary re-crystallization in the materials sintered at 1360 °C and the ensuing internal stresses. Broadband permeability and energy loss behaviors are analyzed by separating the contributions of the different intrinsic loss mechanisms, eddy currents and spin damping, and the types of magnetic processes, domain wall displacements and magnetization rotations. Based on the idea that, within the low induction regimes belonging to the Rayleigh region, the rotational permeability is independent of the peak polarization value J_p , it is shown by simple self-consistent argument that rotational and d.w. permeabilities can be separated across the whole investigated DC – 1 GHz frequency range. It is then found that both d.w. and rotational permeabilities decrease upon the 1360 °C sintering process, their shape revealing relaxation and resonant character, respectively. It is also observed that eddy current losses play a role in the 5mm thick

ring samples only beyond a few MHz. Once they are expunged by reducing the ring thickness down to about 1.2 mm, the experimental $W(f)$ curves of different sample types coalesce into a single curve. This is actually what modeling of rotational losses by spin damping eventually predicts. With this model, real and imaginary permeabilities versus frequency are found within the usual framework of the Landau-Lifshitz-Gilbert equation, where the internal anisotropy fields are assumed to be distributed in amplitude and direction, giving rise to a distribution of resonance frequencies. It is in particular verified that beyond a few MHz the behavior of $W(f)$ can be justified in terms of distribution of the internal demagnetizing fields widening with the frequency, as a result of progressive overcoming of the local resonant frequencies. Rotational and d.w. loss contributions are then separated, the latter dominating the lower frequency range and decaying rapidly in favor of the former beyond a few hundred kHz.

ACKNOWLEDGMENT

One of the authors (S. Dobák) acknowledges support by the project KVARK (ITMS 26110230084), financed through the European Social Fund and by the project VEGA 1/0330/15 of the Scientific Grant Agency of the Ministry of Education, Science, Research and Sport of the Slovak Republic and the Slovak Academy of Sciences.

REFERENCES

- [1] H. Pascard, “Basic concepts for high permeability in soft ferrites,” *J. Phys. France* **8** (1998) 377-384.
- [2] J. Hanuszkiewicz, D. Holz, E. Eleftheriou, and V. Zaspalis, “Materials processing issues influencing the frequency stability of the initial magnetic permeability of MnZn ferrites,” *J. Appl. Phys.* **103** (2008) 103907.

- [3] M.T. Johnson and E.G. Visser, "A coherent model for the complex permeability in polycrystalline ferrites," *IEEE Trans. Magn.* 26 (1990) 1987-1989.
- [4] R. Lebourgeois, C. Le Fur, M. Labeyrie, M. Paté, J-P. Ganne, "Permeability mechanisms in high-frequency polycrystalline ferrites," *J. Magn. Magn. Mater.* 160 (1996) 329-332.
- [5] Yapi Liu and Sijin He, "Development of low-loss Mn-Zn ferrite working at frequency higher than 3 MHz," *J. Magn. Magn. Mater.* 320 (2008) 3318-3322.
- [6] T. Tsutaoka, "Frequency dispersion of complex permeability in Mn-Zn and Ni-Zn spinel ferrites and their composite materials," *J. Appl. Phys.* 93 (2003) 2789-2796.
- [7] V. Babayan, N.E. Kazantseva, R. Moučka, I. Sapurina, Yu.M. Spivak, V.A. Moshnikov, "Combined effect of demagnetizing field and induced magnetic anisotropy on the magnetic properties of manganese-zinc ferrite composites," *J. Magn. Magn. Mater.* 324 (2012) 161-172.
- [8] T. Tsutaoka, T. Kasagi, K. Hakateyama, M.Y. Koledintseva, "Analysis of the permeability spectra of spinel ferrite composites using mixing rules," *IEEE Proc. Int. Symp. EMC* (2013) 545-550.
- [9] S. Yamada, and E. Otsuki, "Analysis of eddy current loss in Mn-Zn ferrites for power supplies," *J. Appl. Phys.* 81 (1987) 4791-4793.
- [10] Ke Sun, Zhongwen Lan, Zhong yu, Zhiyong Xu, Xiaona Jiang, Zihui Wang, Zhi Liu, and Ming Luo, "Temperature and frequency characteristics of low-loss Mn-Zn ferrite in a wide temperature range," *J. Appl. Phys.* 109 (2011) 106103.
- [11] D. Stoppels, "Developments in soft magnetic power ferrites," *J. Magn. Magn. Mater.* 160 (1996) 323-328.
- [12] V. Loyau, G.-Y. Wang, M. Lo Bue, and F. Mazaleyrat, "An analysis of Mn-Zn ferrite microstructure by impedance spectroscopy, scanning transmission electron microscopy and energy dispersion spectrometry characterization," *J. Appl. Phys.* 111 (2012) 053928.
- [13] F. Fiorillo, C. Beatrice, O. Bottauscio, A. Manzin, and M. Chiampi, "Approach to magnetic losses and their frequency dependence in Mn-Zn ferrites," *Appl. Phys. Lett.*, 89 (2006) 122513.
- [14] F. Fiorillo, C. Beatrice, O. Bottauscio, E. Carmi, Eddy current losses in Mn-Zn ferrites, *IEEE Trans. Magn.* 50 (2014) 6300109.
- [15] F. Fiorillo and C. Beatrice, "A comprehensive approach to broadband characterization of soft ferrites," *Int. J. Appl. Electromagnetics Mechanics*, 48 (2015) 283-294.
- [16] V.T. Zaspalis, E. Antoniadis, E. Papazoglou, V. Tsakaloudi, L. Nalbandian, and C.A. Sikalidis, "The effect of Nb₂O₅ dopant on the structural and magnetic properties of Mn-Zn ferrites," *J. Magn. Magn. Mater.* 250 (2002) 98-109.
- [17] R. Morineau and M. Paulus, "Chart of PO₂ versus temperature and oxidation degree for Mn-Zn ferrites in the composition range: 50 < Fe₂O₃ < 54; 20 < MnO < 35; 11 < ZnO < 30 (mole %)," *IEEE Trans. Magn.* 5 (1975) 1312-1314.
- [18] A. Caprile, M. Coisson, F. Fiorillo, P. Kabos, O.M. Manu, E. S. Olivetti, M.A. Olariu, M. Pasquale, and V. A. Scarlatache, "Microwave behavior of polymer bonded iron oxide nanoparticles," *IEEE Trans. Magn.* 48 (2012) 3394-3397.
- [19] J. Smit and H.P.J. Wijn, *Ferrites*, Eindhoven: Philips Technical Library, 1959, p. 236.
- [20] H. Suhl, "Theory of the magnetic damping constant", *IEEE Trans. Magn.* 34 (1988) 1834-1838.
- [21] F. Fiorillo, E. Ferrara, M. Coisson, C. Beatrice, and N. Banu, "Magnetic properties of soft ferrites and amorphous ribbons up to radiofrequencies," *J. Magn. Magn. Mater.* 322 (2010) 1497-1504.

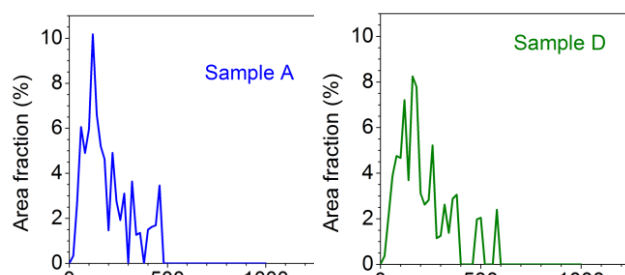


Fig. 1 – Distribution of the area fraction of the grains obtained by SEM analysis in Mn-Zn ferrite samples sintered at: 1325 °C -3 hours (A), 1340 °C-3hours (D); 1360 °C-3hours (G); 130 °C-7 hours (I).

- 12 Table 1 – Physical parameters of the selected Mn-Zn ferrite ring samples. T_s \equiv sintering temperature; t_s \equiv sintering time; δ \equiv mass density; $\langle s \rangle$ \equiv average grain size; σ_{DC} \equiv DC conductivity; σ_{10MHz} \equiv conductivity at 10 MHz; J_s \equiv saturation polarization.

Sample	T_s (°C)	t_s (hours)	δ (kg/m ³)	$\langle s \rangle$ (μm)	σ_{DC} (Ω ⁻¹ m ⁻¹)	$\sigma_{10\text{ MHz}}$ (Ω ⁻¹ m ⁻¹)	J_s (T)
A	1325	3	4830	11.4	0.146	56.8	0.55
D	1340	3	4850	12.3	0.214	82	0.55
G	1360	3	4900	15.1	0.220	80	0.55
I	1360	7	4890	19.8	0.215	71	0.55

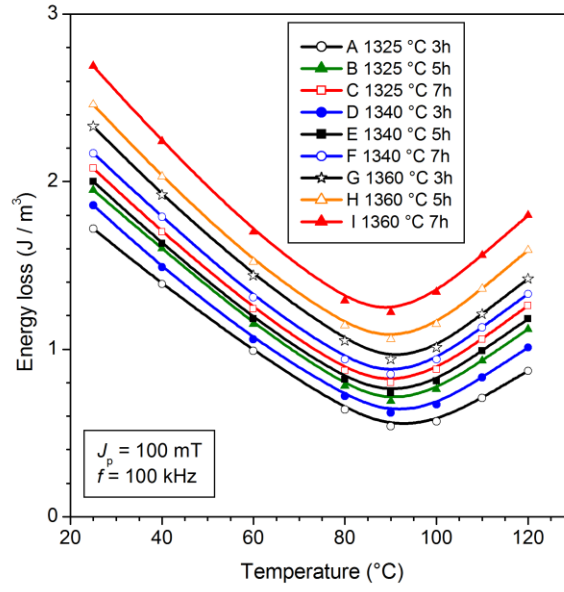


Fig. 2 – Energy loss versus measuring temperature at peak polarization $J_p = 100$ mT and frequency $f = 100$ kHz and its evolution with sintering temperature ($T_s = 1325$ °C, 1340 °C, 1360 °C) and time ($t_s = 3$ hours, 5 hours, 7 hours).

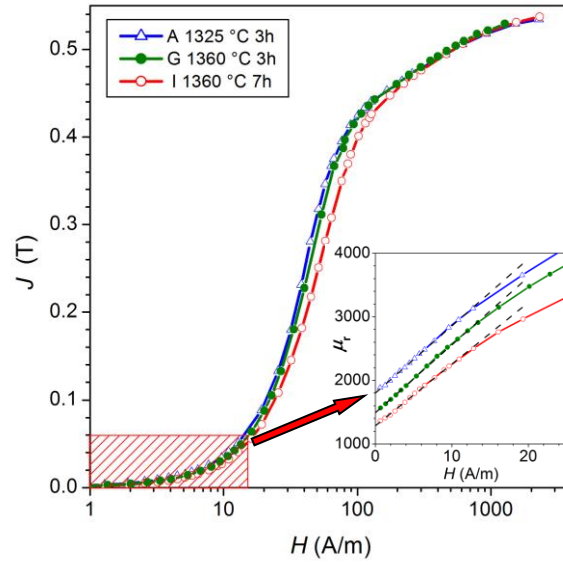


Fig. 3 – Normal magnetization curves measured on two samples subjected to the two extremes of the sintering conditions (sample A, 3 hours at $T_s = 1325$ °C and sample I, 7 hours at $T_s = 1360$ °C) and one sample subjected to intermediate treatment (sample G, 3 hours at $T_s = 1360$ °C). The hatched area identifies the Rayleigh region, where the permeability follows the law $\mu = a + bH$, as sketched in the inset.

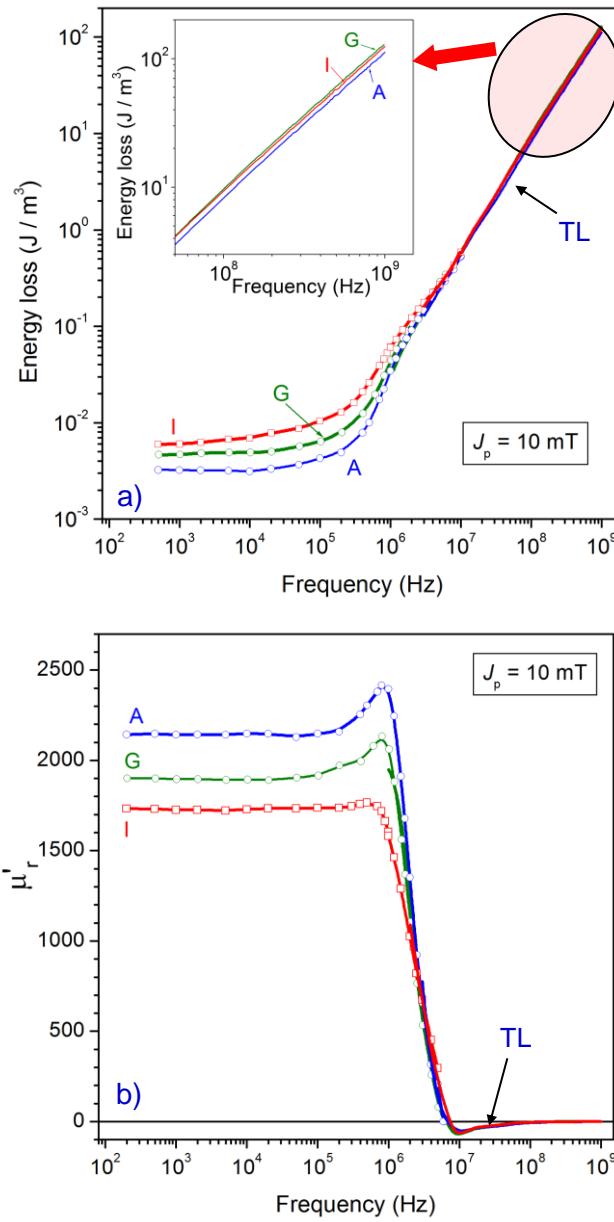


Fig. 4 – a) Energy loss versus frequency measured at $J_p = 10$ mT in the samples A, G, and I. The loss curves tend to coalesce beyond a few MHz. Slight differences are, however, put in evidence in the upper frequency region (see inset). They are related to corresponding differences of the sample conductivity at high frequencies (Table 1). It is noted the superposition of the loss values obtained by the fluxmetric (symbols) and transmission line (TL, continuous curves) methods in the overlapping measuring region 3 MHz – 10 MHz. b) Associated behavior of the relative real permeability μ'_r .

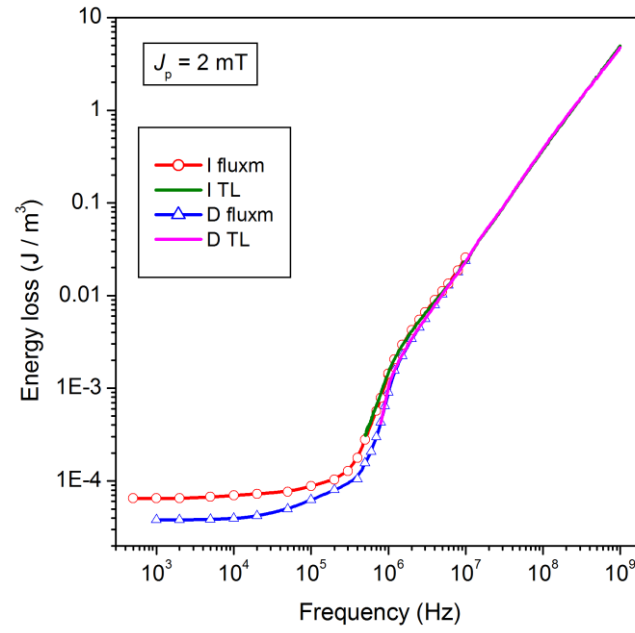


Fig. 5 – Energy loss versus frequency in samples D and I at $J_p = 2 \text{ mT}$. The direct fluxmetric measurements (symbols) and the TL results (continuous lines) obtained according to (1) coincide beyond about 500 kHz.

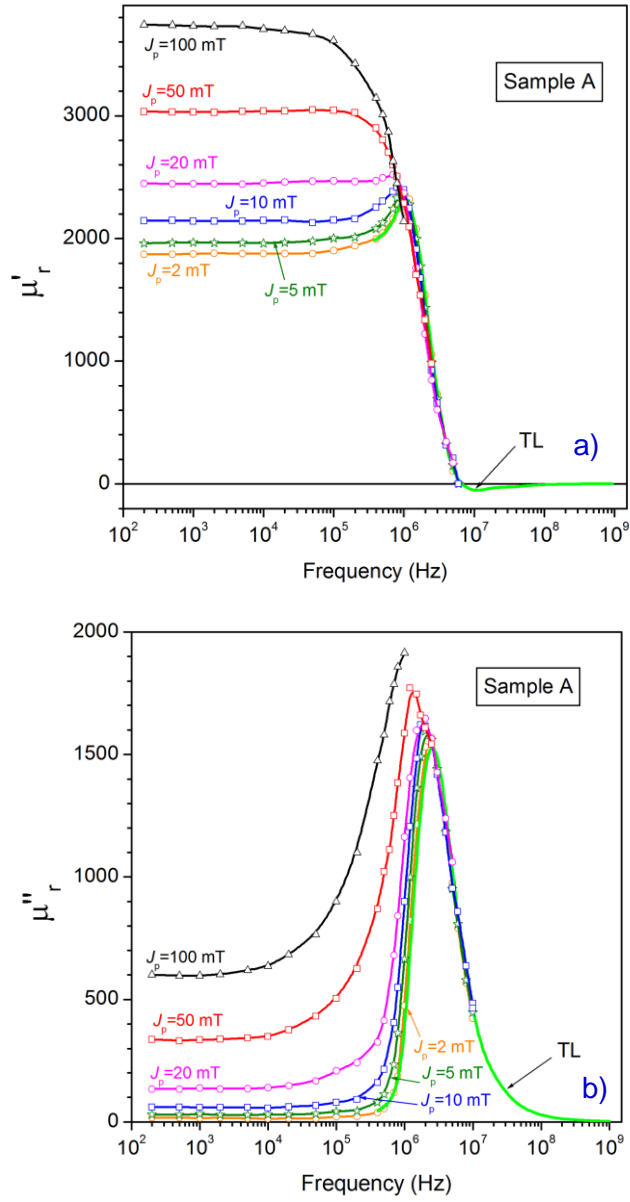


Fig. 6 – a) Real permeability μ'_r versus frequency measured at different J_p values in sample A. All curves taken within the Rayleigh region (i.e. up to $J_p = 50$ mT) coalesce on a single curve in the upper frequency range, because of d.w. relaxation. b) Same as a) for the imaginary permeability μ''_r .

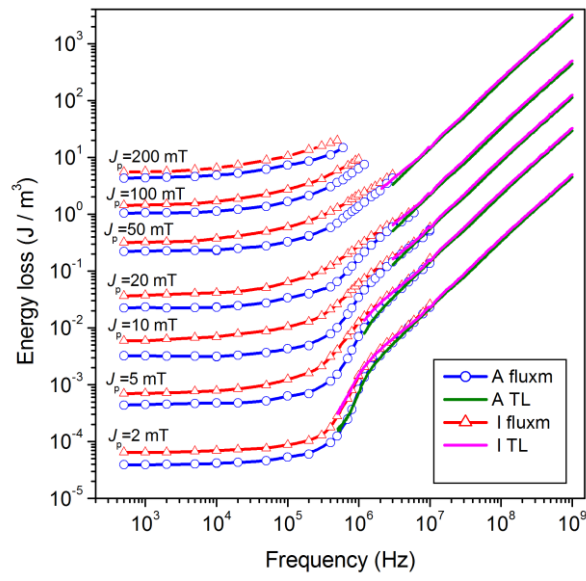


Fig. 7 – Comparison of broadband energy loss behavior of the A and I samples. The more defective microstructure of the I sample, hindering the domain wall processes, is reflected in higher quasi-static and medium frequency losses. The slight difference observed at the highest frequencies is related to correspondingly higher high-frequency conductivity of sample I (see Table 1).

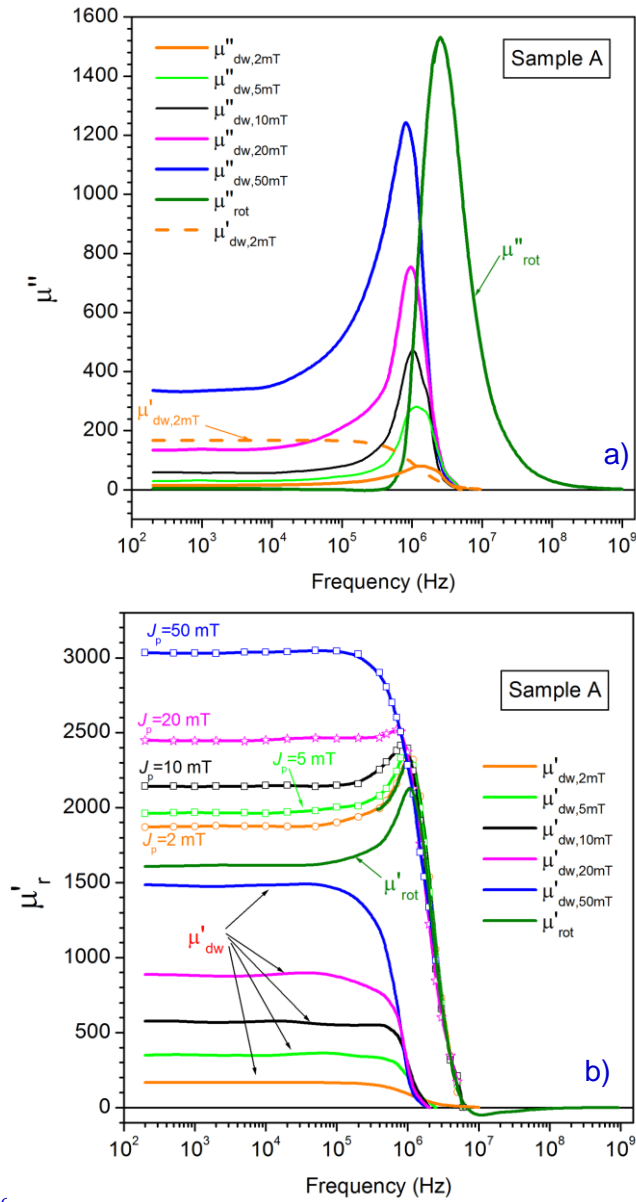


Fig. 8 – Sample A: separation of imaginary $\mu''(f)$ and real $\mu'(f)$ permeabilities into d.w. μ''_{dw} and rotational μ''_{rot} components for J_p ranging between 2 mT and 50 mT. The behavior of the measured $\mu'(f)$ is provided for comparison. It is remarked that the rotational components $\mu'_{rot}(f)$ and $\mu''_{rot}(f)$ are independent of J_p .

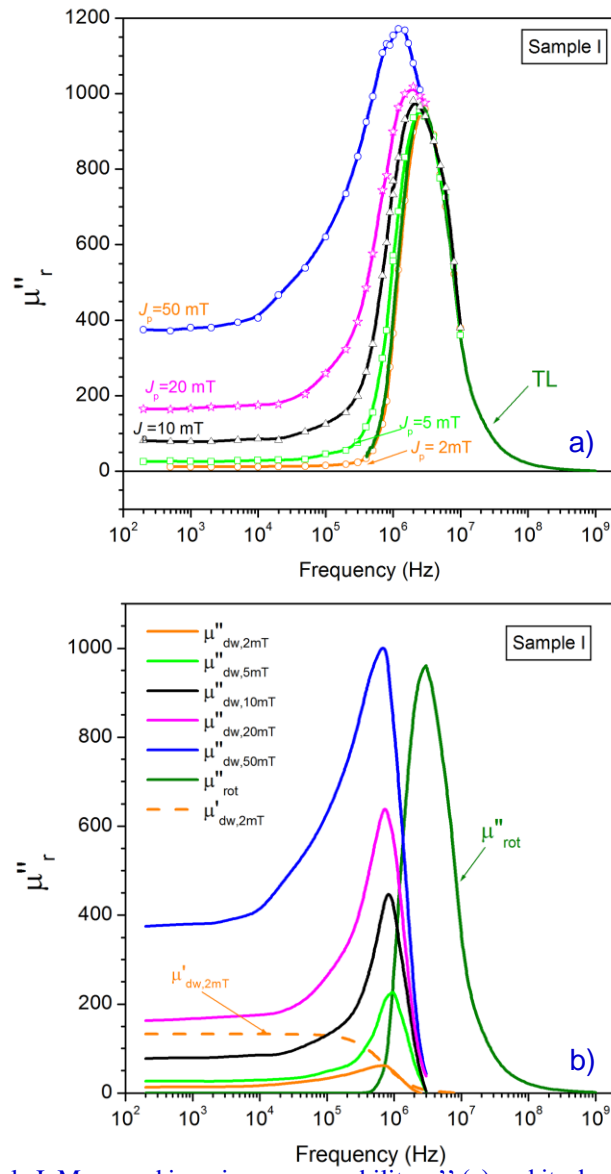


Fig. 9 – Sample I. Measured imaginary permeability μ'' (a) and its decomposition (b) into d.w. μ''_{dw} and rotational μ''_{rot} components.

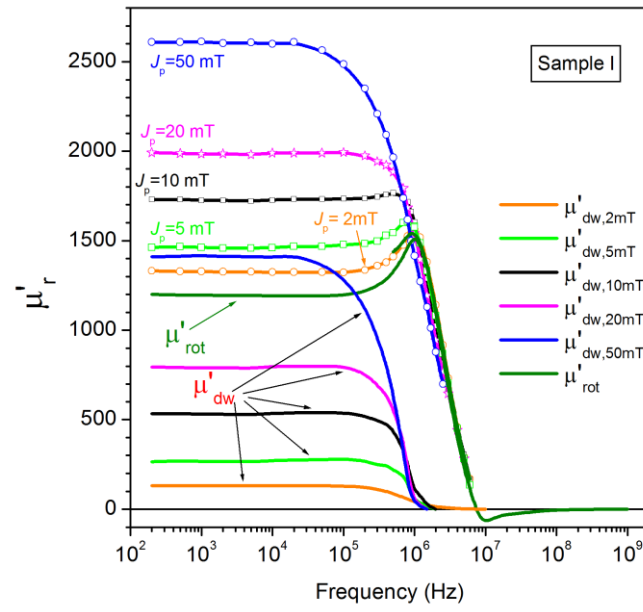


Fig. 10 – Sample I. Measured real permeability $\mu'_r(f)$ and its calculated components $\mu'_{dw}(f)$ and $\mu'_{rot}(f)$.

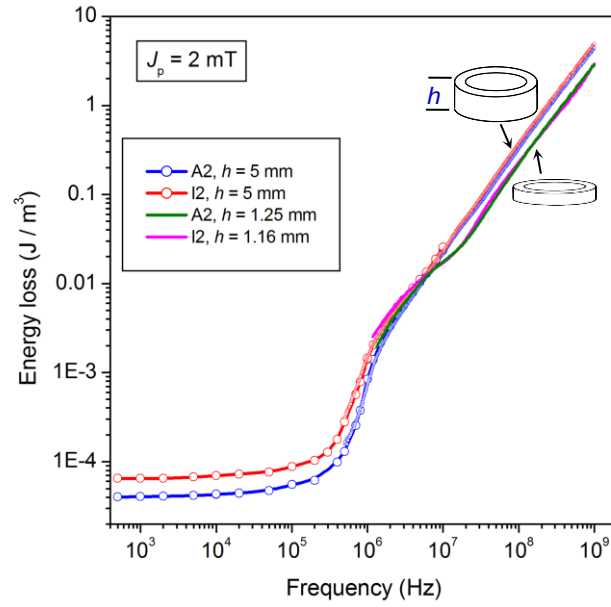


Fig. 11 – Energy loss measured at $J_p = 2 \text{ mT}$ in samples A and I before and after thinning. The $W(f)$ curves on the 5mm thick rings slightly differ at high frequencies, because of different high frequency conductivities (Table 1). The eddy current loss $W_{\text{eddy}}(f)$ comes to light after thinning. It can be appreciated above about 5 MHz. Above this frequency the eddy-current-free curves collapse into a single curve.

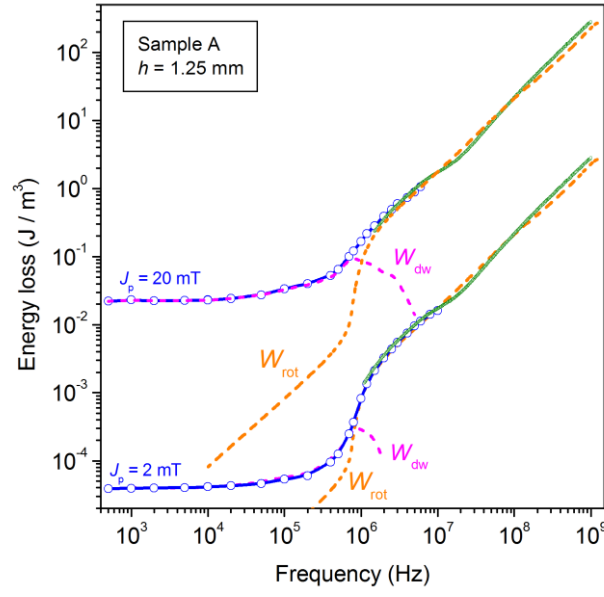


Fig. 12 – Energy loss $W(f)$ measured at $J_p = 2$ mT and $J_p = 20$ mT in the thin eddy-current-free sample A and predicted decomposition in the rotational $W_{\text{rot}}(f)$ and d.w. $W_{\text{dw}}(f)$ contributions (dashed lines). The remarkable difference observed between the behaviors of $W(f)$ for $J_p = 2$ mT and $J_p = 20$ mT at intermediate frequencies descends from the different relative proportions of $W_{\text{rot}}(f)$ and $W_{\text{dw}}(f)$ at different J_p values.

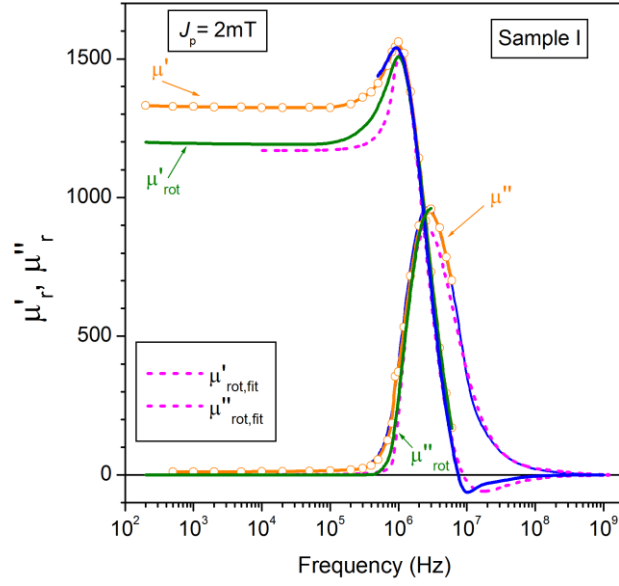


Fig. 13 – Sample I. Rotational permeabilities μ'_{rot} and μ''_{rot} obtained from the measured permeabilities according to the procedure discussed in Section IV and its prediction by Eqs. (7a) and (7b) (dashed lines).

